

Microstructural evolution in laser-ablation-deposited Fe–25 at.% Ge thin film

Krishanu Biswas^{a)}

Department of Metallurgy, Indian Institute of Science, Bangalore 560012, India

Puspendu Kumar Das

Department of Inorganic and Physical Chemistry, Indian Institute of Science, Bangalore 560012, India

Kamanio Chattopadhyay

Department of Metallurgy, Indian Institute of Science, Bangalore, 560012, India

(Received 10 February 2005; accepted 3 October 2005)

Films with Fe–25 at.% Ge composition are deposited by the process of laser ablation on single crystal NaCl and Cu substrates at room temperature. Both the vapor and liquid droplets generated in this process are quenched on the substrate. The microstructures of the embedded droplets show size as well as composition dependence. The hierarchy of phase evolution from amorphous to body-centered cubic (bcc) to DO₃ has been observed as a function of size. Some of the medium-sized droplets also show direct formation of ordered DO₁₉ phase from the starting liquid. The evolution of disordered bcc structure in some of the droplets indicates disorder trapping during liquid to solid transformation. The microstructural evolution is analyzed on the basis of heat transfer mechanisms and continuous growth model in the solidifying droplets.

I. INTRODUCTION

The formation of coatings and thin films using pulsed laser ablation process is increasingly gaining importance.^{1–4} The rapid superheating at the subsurface due to coupling and transfer of energy from the laser beam to the target materials leads to catastrophic vaporization and explosion resulting in generation of atomized droplets in addition to the vapor plasma. The vapor plasma and the liquid droplets move at high speed (~10–100 ms⁻¹)⁵ and are quenched on a suitably positioned substrate. This technique allows us to study the microstructure of the film as well as the liquid droplets, which solidify under nonequilibrium conditions.

In this paper, we report such a study on Fe–25 at.% Ge alloy. The iron rich Fe–Ge alloys show strong tendency to order. The phase diagram is shown in Fig. 1.⁶ According to this diagram, on cooling a liquid of Fe–25 at.% Ge composition, the first phase that forms from the liquid is α_2 having B2 ordered structure ($a = 0.28815$ nm). This phase upon further cooling transforms to ϵ (DO₁₉, $a = 0.5169$ nm, $c = 0.4222$ nm) by a peritectic reaction with

the remaining liquid at 1395 K. The ϵ phase further transforms to ϵ' and $\alpha_1 + \beta$ phase at 973 and 673 K respectively. The ϵ' phase has an ordered face-centered cubic (fcc)-based cubic structure (L1₂, $a = 0.3665$ nm) whereas α_1 is body-centered cubic (bcc)-based ordered structure (DO₃, $a = 0.5763$ nm). The β phase has hexagonal structure (B8₂, $a = 0.3998$ nm and $c = 0.501$ nm).

The motivation of the present investigation comes from our recent studies on deeply undercooled Fe–25 at.% Ge alloys.⁷ The rapid solidification of the undercooled Fe–25 at.% Ge alloy droplets (mass ~1 gm and size ~6–7 mm diameter) by the method of electromagnetic levitation technique leads to the formation of α_2 as the primary phase. The α_2 phase has been found to nucleate as the primary phase even at very large undercoolings where direct nucleation of ϵ phase should be possible. The ϵ phase can form either by peritectic reaction (at low levels of undercooling) or by solid-state transformation. These suggest strong nucleation barriers for the formation of the ϵ phase during undercooling experiments. The aim of the present investigation is to study the microstructural evolution in atomized droplets during the process of laser ablation. These atomized droplets are much smaller than the droplets used for the undercooling experiments.⁷ Therefore, possible larger departure from equilibrium may lead to the formation of various metastable phases. No report is available indicating glass

^{a)}Address all correspondence to this author.

e-mail: kris@met.iisc.ernet.in

DOI: 10.1557/JMR.2006.0023

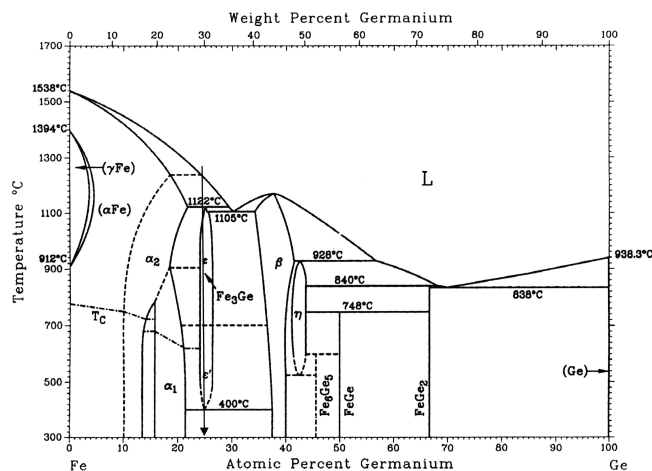


FIG. 1. Equilibrium phase diagram of the Fe–Ge system.⁶ The arrow marks the composition of the target used for the study.

formation in this binary alloy during rapid solidification. However, driven processes like mechanical milling of Fe–Ge blends with Ge < 27 at.% as well as ϵ -Fe₃Ge and ϵ' -Fe₃Ge intermetallics reported to form disordered bcc solid solution.⁸

II. EXPERIMENTAL

A. Sample preparation

The alloy target (cylindrical tablet of 1.5 cm diameter and 0.5 cm thickness) was prepared by arc melting high purity iron (99.9 %) and germanium (99.99 %). The alloy was homogenized by repeated melting prior to its final shaping by grinding. The details of the ablation set up are given elsewhere.⁹ A Q-switched Nd-yttrium aluminum garnet (YAG) (INDI, Spectra Physics) laser with peak energy of 450 mJ/pulse was used for the ablation study. The deposition parameters are given in Table I. The starting vacuum level in the chamber was kept in the range of 10^{-7} mbar. For plan view transmission electron microscopic (TEM) study, the time for deposition was 7 min. This yields 20–40-nm-thick film on the NaCl substrate. After deposition on NaCl substrates, the films were floated by dissolving NaCl in double-distilled water, and

TABLE I. Process parameters for film deposition.

Laser power	225 mJ/pulse
Pulse width	5–8 ns
Frequency	10 Hz
Spot size	1.2 mm diameter
Target	Fe–25 at.% Ge
Substrates	Pure Cu and NaCl
Target to substrate distance	20 mm
Substrate temperature	300 K

the floated film fragments were collected on 400 mesh copper grid for direct observation in TEM. For scanning electron microscopic (SEM) observations, thicker films were deposited on clean and flat high purity (99.9%) copper substrates. In this case the deposition time used was 30 min.

B. Characterization of films

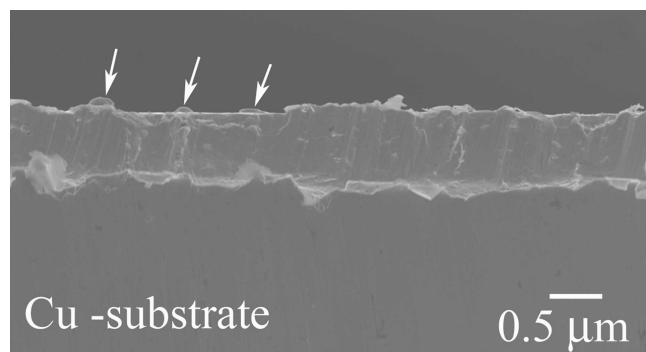
The detailed microstructural analysis of films was carried out using transmission electron microscope (TEM; JEOL 2000 FXII) operating at 200 kV and scanning electron microscope (SEM; JEOL JSM 830A) operating at 20 kV. The compositional analyses of the embedded droplets were carried out using energy dispersive x-ray analyzer (EDS; Oxford) attached to both SEM and TEM. In the case of TEM, compositional measurements were performed in TEM mode by reducing the beam to the desired size. This technique permitted the position of the analyzed zone to be localized precisely. The Cliff–Lorimer ratio technique¹⁰ was used in this case. To ensure a sufficient statistical precision, a counting time varying from 2 to 3 min was used. No drift was detectable during this acquisition time. The excellent vacuum ($<10^{-7}$ Torr) in the microscope reduced the contamination of the probe to an acceptable limit.

III. RESULTS

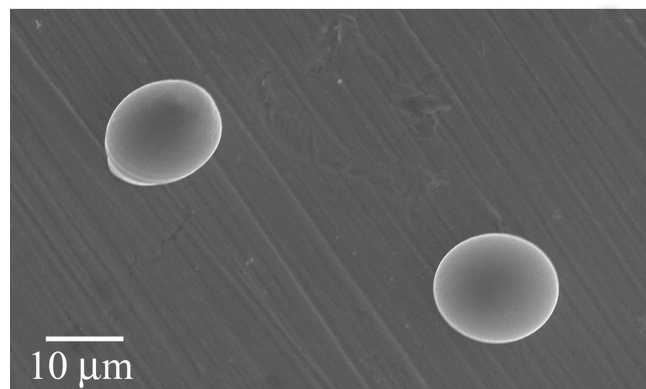
The as-deposited films contain smooth matrix in which spherical particles are embedded. Figure 2(a) shows the cross-sectional view of the film deposited on copper substrate. The presence of hemispherical droplets, which are sticking on the film surface and protruding outward, can be clearly seen. Some of the droplets are marked by white arrows. The low magnification secondary electron image showing plan view of the as-deposited film is shown in Fig. 2(b). It reveals the presence of spherical droplets in a smooth background of the film.

A. Composition analysis of the droplets

The compositions of the droplets have been measured by EDS attached to both SEM and TEM. The composition of droplets as a function of size as measured in the SEM is shown in Fig. 3(a). For droplets with larger sizes, the compositions are close to the overall composition of the film. However, at smaller sizes, the compositions show a scatter with most of the droplets exhibiting depletion of germanium. To establish the trend, EDS analysis of the smaller particles are carried out using TEM [Fig. 3(b)]. While measuring the compositions of the droplets, the beam size was always kept smaller than the size of the droplet. The results show increase in iron content and larger scatter at smaller sizes. For particles ~100 nm size, the composition varies from 10 to



(a)



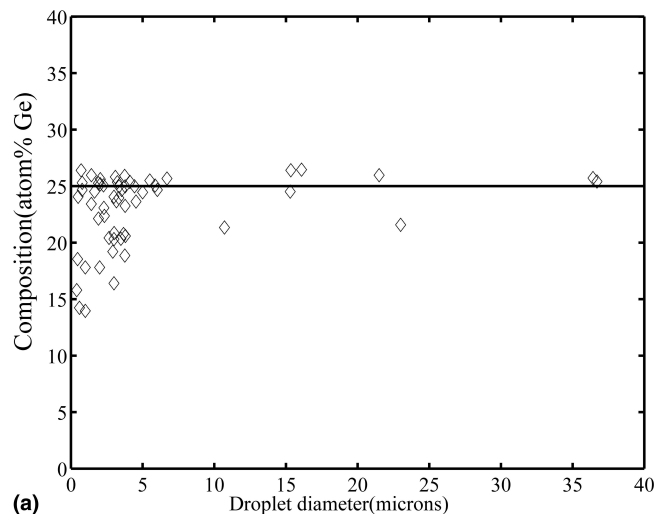
(b)

FIG. 2. SEM micrographs: (a) showing cross-sectional view of the film deposited on copper substrate; (b) plan view of film deposited on copper substrate showing spherical droplets. The white arrows in (a) mark the presence of the spherical droplets.

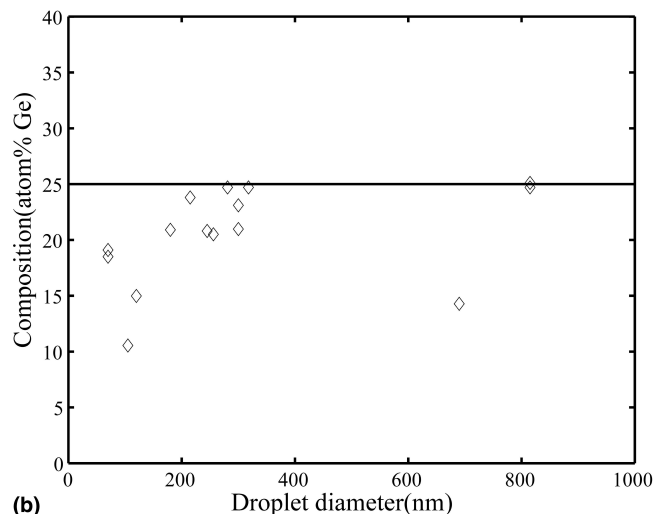
18 at.% Ge. However, with the increasing size, they rapidly converge and above a size of 400 nm, the composition is same as the embedding matrix (~25 at.% Ge).

B. Phase formation in the embedded particles

The embedded droplets can be broadly classified into four size ranges: approximately 70, 100–200, 200–500, and 500 nm and above. Figure 4(a) shows typical bright-field micrograph of a fine droplet (~70 nm). The droplet has a composition of Fe–19 at.% Ge and exhibiting granular contrast suggesting amorphous nature. The darker contrast of the droplet compared to the film is due to absorption through the greater thickness of the droplet than the film. Figure 4(b) shows bright-field image of the same droplet after it has been tilted at an angle of 30° from the setting of Fig. 4(a). The granular contrast of the droplet remains unchanged. No evidence of diffraction contrast could be obtained during tilting. This further confirms the absence of any crystalline phase in the droplet. The selected area diffraction (SAD) pattern taken from the droplet [as shown in the inset of Figs. 4(a) and 4(b)] also corroborates the amorphous nature of the droplet. In contrast, Fig. 4(c) shows the bright-field image of a droplet of similar size (~70 nm) and composition



(a)



(b)

FIG. 3. Compositions of droplets as a function of droplet diameter measured by EDS attached to (a) SEM and (b) TEM.

(Fe–18.5 at.% Ge) exhibiting crystalline nature. The micro-diffraction pattern along [001] direction taken from the small grain [as shown as the inset of Fig. 4(c)] indicates that the structure is disordered bcc.

Each spherical droplet in the size range 100–200 nm contains multiple small grains [Fig. 5(a)]. These grains have a composition of ~Fe–21 at.% Ge as measured by EDS. The micro-diffraction patterns taken from one such grain are shown in Figs. 5(b) and 5(c). The [001] zone axis pattern again indicates a disordered bcc structure.

The droplets in the size range of 200–500 nm mostly exhibits polycrystalline grains (~50–80 nm in size) as shown in Fig. 6(a) with composition close to Fe–25 at.% Ge (23.5–25 at.% Ge). The analysis of micro-diffraction patterns reveals a disordered bcc structure [Figs. 6(b) and 6(c)]. Occasionally, some of the droplets show larger grains (often bicrystal), as shown in Fig. 7(a). The micro-diffraction patterns taken from the two grains are shown in Figs. 7(b) and 7(c). These patterns can be indexed in

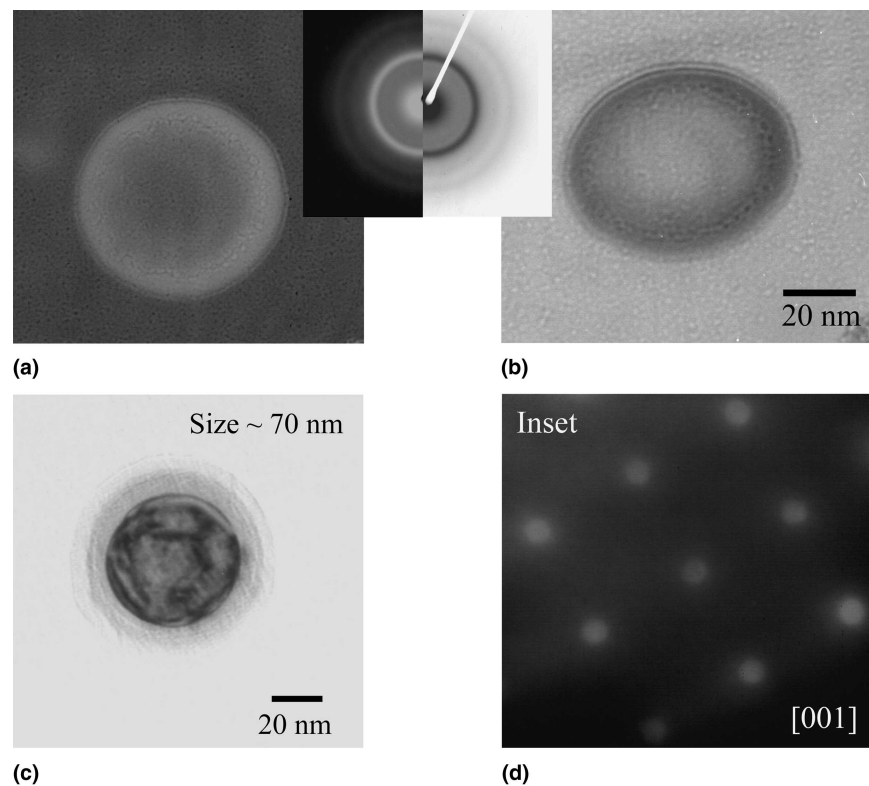


FIG. 4. (a) Bright-field image of a 70-nm-diameter droplet showing fine granular contrast at zero-tilt condition, (b) the same droplet with x-tilt = 30° with inset showing the SAD pattern taken from the droplet, and (c) bright-field image of another 70-nm-diameter droplet with inset showing micro-diffraction pattern along [001] zone axis of bcc α -FeGe.

terms of the ordered ϵ (DO_{19}) phase. The composition of the droplets larger than 500 nm is close to the target composition (Fe–25 at.% Ge). The microstructure indicates the presence of multiple grains with grains often growing from the droplet/matrix interface as shown in Figs. 8(a) and 8(b). The [001] and [011] micro-diffraction patterns [shown in Figs. 8(c) and 8(d)] from these grains indicate an ordered DO_3 structure.

IV. DISCUSSION

A. Solidification of the embedded particles

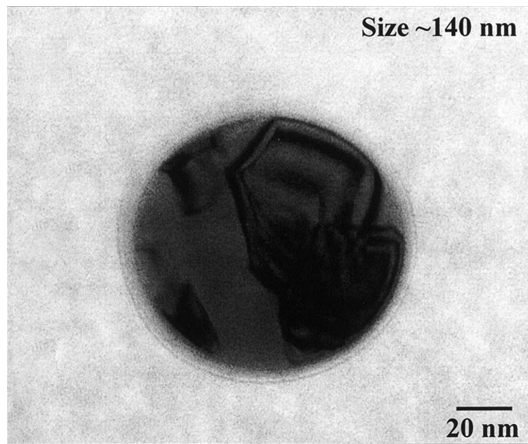
As discussed in the introduction, motivation for studying the ablated particles in the laser ablation process is to understand the phase selection processes during the solidification of Fe–Ge alloy with near Fe_3Ge composition. The levitation experiments indicate that in the highly undercooled droplets of several millimeters diameter having similar compositions, ordered α_2 is always the first phase to nucleate. It transforms into ϵ phase either by a peritectic reaction (at low levels of undercooling) with liquid or through a solid state transformation.⁷

The present experiments attempt to address the question of phase selection in still smaller droplets produced during laser ablation. There are two added effects, which may influence phase selection with reduced droplet size.

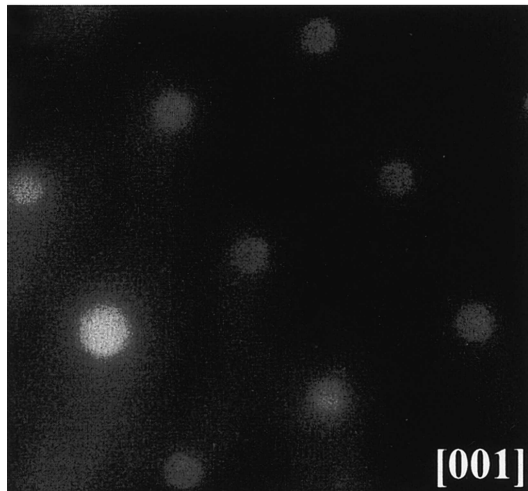
The first one is the isolation of the heterogeneous nucleation sites that may exist in the melt. For a given distribution of these sites in a given volume of melt, fragmentation of it into smaller sizes leads to the segregation of these sites to few particles leaving the others free to undercool. In case of sufficiently large levels of undercooling, the particles can undergo homogeneous nucleation. Alternatively, either the impinging substrate or embedding matrix can trigger heterogeneous nucleation. A second effect, which can influence the phase selection, is the rapid heat transfer experienced by the melt as the particles impinge the substrate and become surrounded by the matrix phase. The increased heat transfer can lead to a kinetically controlled phase selection process where some of the nucleation events can be bypassed due to high cooling rate. We will discuss the phase selection issues coupled with heat transfer in the next two sections. First we will discuss the calculation of heat transfer in the droplets.

1. Heat transfer in the droplets

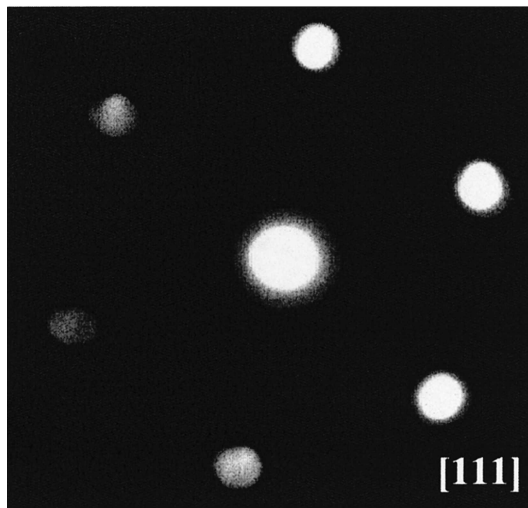
The fluid dynamics and heat transfer phenomena that occur when a liquid metal droplet falls on a cold substrate have been studied extensively in the literature.^{11–13} In the present case, the problem can be defined in the following way. A liquid metal droplet, originally spherical shape



(a)

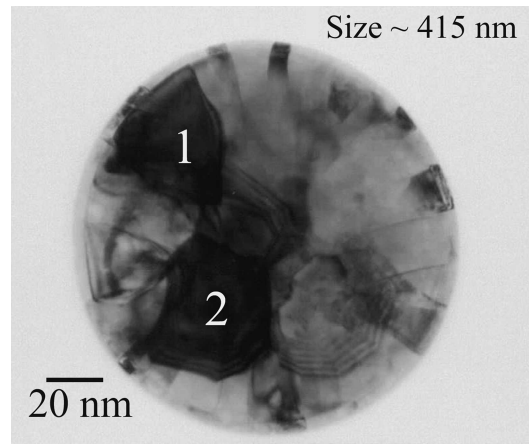


(b)

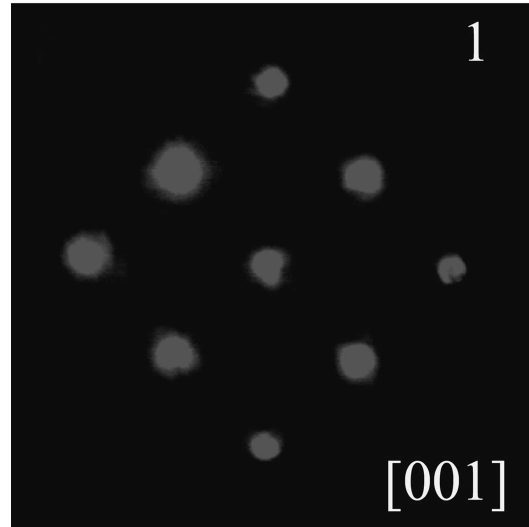


(c)

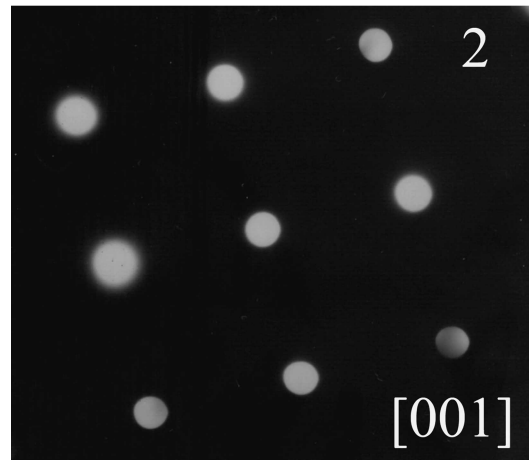
FIG. 5. (a) Bright-field image of a 140-nm-sized droplet showing a number of grains, (b) [001], and (c) [111] micro-diffraction patterns showing absence of super lattice reflections.



(a)

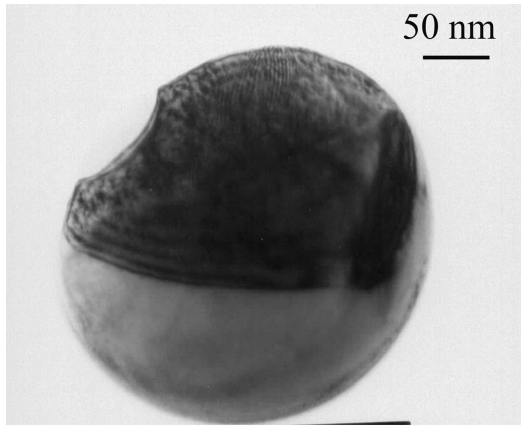


(b)

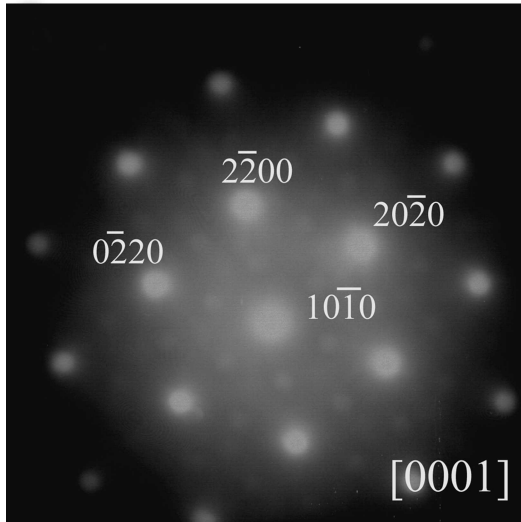


(c)

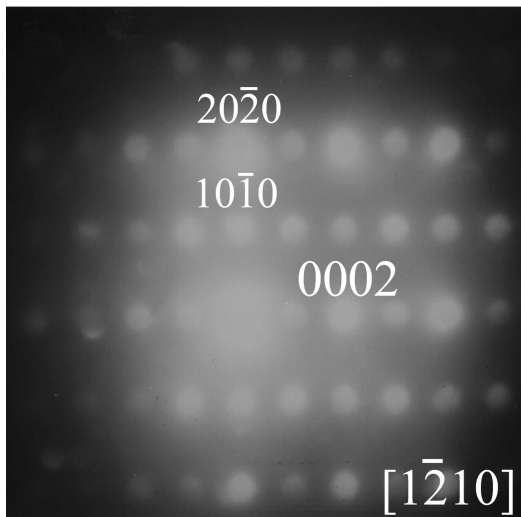
FIG. 6. (a) Bright-field image of another medium-sized droplet showing a number of grains, (b) SADP showing rings corresponding to bcc reflections of α -FeGe, and (c) [001] micro-diffraction patterns taken from grains marked as 1 and 2 showing absence of super lattice reflections.



(a)



(b)



(c)

FIG. 7. (a) Bright-field image of a medium sized droplet showing two grains, (b) and (c) micro-diffraction patterns showing the [0001] and [1̄2̄10] zone axes patterns of ϵ . The presence of super-lattice reflections can be observed.

with radius r_0 , moves toward the flat substrate with initial velocity, v_0 during the expansion of plasma containing the droplets as well as vapor. After the droplet makes an impact with the substrate surface, it spreads out and is flattened. In the meantime, it is cooled down by the substrate and solidifies. The heat transfer in the liquid droplet involves conduction coupled with convection whereas heat transfer in the substrate is unsteady conduction only. The thin film deposition process takes place inside a vacuum chamber with starting vacuum level of 10^{-7} Torr. Therefore, we can ignore the convective heat transfer from the droplet surface to the surrounding gas molecules. The heat transfer during the flight of the droplet from the target surface to the substrate surface prior to the impact is by the process of radiation only. The velocity with which plasma containing atomized droplets moves toward the substrate surface has been found to be $10\text{--}100\text{ ms}^{-1}$.⁵ Considering the normal distance from the target to substrate as 1.5 cm, the time required for the flight is of the order of 10^{-4} to 10^{-3} s. This time scale is quite small as compared to the whole process; we can ignore the heat transfer due to radiation during the flight. The mathematical model used considers the conjugate heat transfer of the droplet and substrate.¹⁴ As the substrate dimensions are sufficiently large as compared to the droplet, we can assume the substrate as isothermal. The Lagrangian formulation is used to model the conjugate heat transfer in the droplet and substrate. The relevant energy conservation equation, initial and boundary conditions are as follows:

The energy equation in the droplet is

$$\frac{\partial \Phi_1}{\partial \tau} = \frac{1}{Pe_1} \left[\frac{\delta}{\delta R} \left(\frac{1}{R} \frac{\partial \Phi_1}{\partial R} \right) + \frac{\partial^2 \Phi_1}{\partial z^2} \right] . \quad (1)$$

The energy equation in the substrate is

$$\frac{\partial \Phi_2}{\partial \tau} = \frac{1}{Pe_2} \left[\frac{\delta}{\delta R} \left(\frac{1}{R} \frac{\partial \Phi_2}{\partial R} \right) + \frac{\partial^2 \Phi_2}{\partial z^2} \right] . \quad (2)$$

The initial condition can be written as

$$\text{at } \tau = 0, \Phi_1(R, Z, 0) = 1, \Phi_2(R, Z, 0) = 0 . \quad (3)$$

The boundary conditions are given as follows at the droplet free surface and substrate boundary:

$$\frac{\partial \Phi_i}{\partial R} n_r + \frac{\partial \Phi_i}{\partial Z} n_z = 0, \quad i = 1, 2 \quad , \quad (4)$$

at the splat/substrate interface,

$$\Phi_1 = \Phi_2, -k_1 \frac{\partial \Phi_1}{\partial z} = -k_2 \frac{\partial \Phi_2}{\partial z} \quad , \quad (5)$$

and in the substrate far from the interface,

$$\Phi_2(R, -\infty, \tau) = \Phi_2(\infty, Z, \tau) = 0 \quad . \quad (6)$$

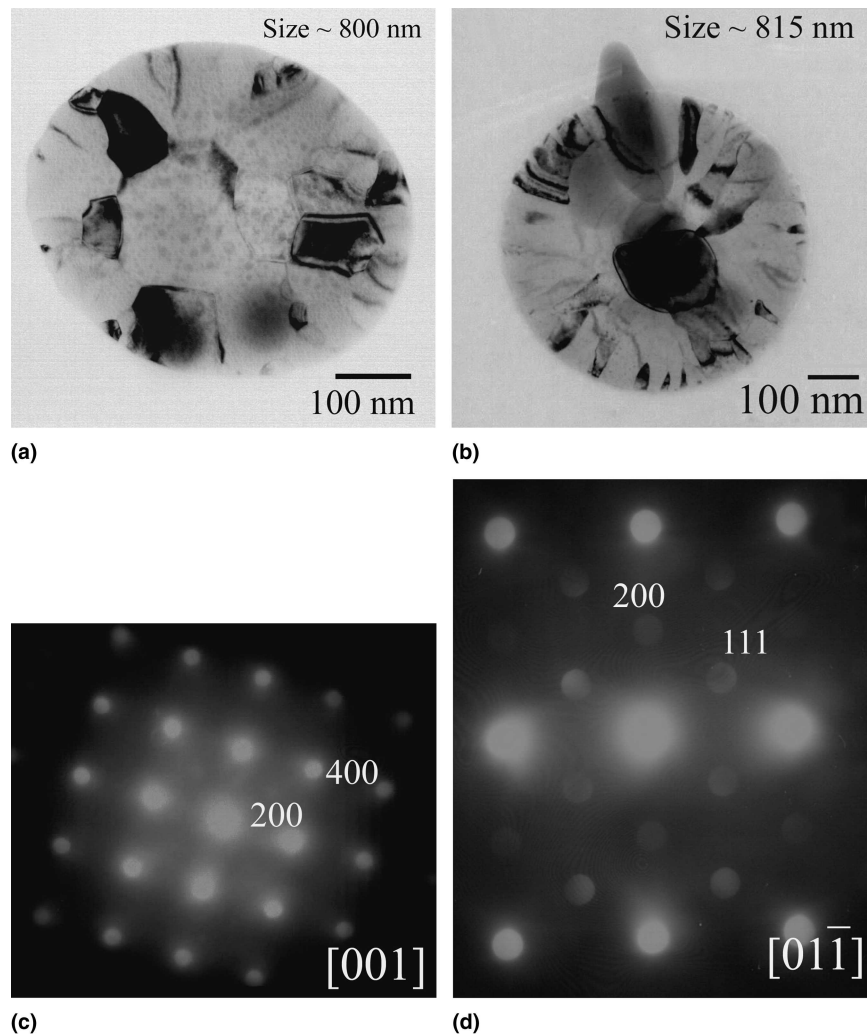


FIG. 8. Bright-field images of an (a) 800-nm-sized droplet, (b) 815-nm-sized droplet showing elongated grain morphology, (c) [001], and (d) [011] micro-diffraction patterns showing super lattice reflections. The presence of super-lattice reflections corresponding to DO_3 can be seen.

The non-dimensionalization has been carried out according to the following definitions: $\Phi_i = [T_i - \min(T_0, T_w)]/|T_0 - T_w|$, $i = 1, 2$ and T_i is temperature of either droplet or substrate. The non-dimensional groups in the energy equations are Péclet numbers for droplet and substrate

$$Pe_1 = \frac{r_0 v_0}{\alpha_1}, Pe_2 = \frac{r_0 v_0}{\alpha_2}.$$

In the above equations T , T_0 , and T_w are the temperature, the droplet initial temperature, and substrate initial temperature, k is thermal conductivity, and α is thermal diffusivity. The subscripts 1, 2 stand for droplet and substrate respectively. The dimensionless time, τ is given by $t/(r_0/v_0)$, where t is the real time. Using the implicit numerical scheme, the conjugate heat transfer equation is solved using Fluent software v.6.2.16 (Fluent Inc.).

The physical constants of the droplet used in the simulation are listed in Table II. The thermophysical

TABLE II. Physical properties used in calculation.

Symbol	Parameter	Fe–20 at.% Ge	Fe–25 at.% Ge
T_1	Liquidus temperature (K)	1573	1513
T_Q	Hypercooling (K)	458.86	484.46
C_{pL}	Specific heat of liquid (J/mol K)	39.0	38.3
C_{pS}	Specific heat of solid (J/mol K)	41.8	41.2
k_L	Thermal conductivity of liquid (W/m K)	30.1	29.7
k_S	Thermal conductivity of solid (W/m K)	73.8	72.7
ρ_L	Density of liquid (gm/cc)	6.67	6.59
ρ_S	Density of solid (gm/cc)	7.18	7.03
σ	Solid-liquid interfacial energy (Jm^{-3})	0.337	0.337

properties of the substrate (NaCl) are taken as density, 2.17 g cm^{-3} ; thermal conductivity, $6.5 \text{ Wm}^{-1} \text{ K}^{-1}$; and specific heat: $48.9 \text{ J mol}^{-1} \text{ K}^{-1}$.¹⁵ The cooling rates of droplet of different diameters are calculated using the time taken by droplet during which the droplet is cooled to room temperature (300 K). This cooling rate is then

plotted as a function of droplet diameter. Figure 9 shows such a plot. The cooling rate is found to scale with the droplet size. The cooling rate is as high as 10^8 – 10^9 Ks⁻¹ for droplets smaller than 100 nm. This rate drops as the droplet size increases and becomes 10^4 Ks⁻¹ for large droplets (10 μm).

2. Glass formation

As stated in Sec. III, in few of the small droplets (less than 70 nm), we were unable to observe any diffraction contrast. This suggests that liquid most likely has undergone glass transition rather than crystallization, illustrating a strong role of the kinetic factors, which are influenced by heat transfer from the droplet to substrate. These smaller particles are iron rich where disordered bcc phase can directly nucleate from the melt. This is the first observation of the glass formation by liquid quenching in Fe–Ge binary system. The ultrafine polycrystalline aggregates, which have been formed in the intermediate sized droplets, hint at a competition between the glass formation and the nucleation of bcc phase. From the result, we can conclude that the droplets of about 70 nm size and below have been cooled sufficiently rapidly to bypass the nose of the time-temperature-transformation (TTT) diagram for homogeneous nucleation of bcc phase. For sizes bigger than this, the cooling rate is not sufficiently enough to bypass the nucleation of bcc phase from the liquid. As the cooling rate scales with droplet size, we can conclude that glass formation from the melt is possible for droplets having sizes below 70 nm. To verify this, we have calculated the TTT curves and estimated the critical cooling rate required to avoid the nucleation of bcc phase.

TTT curves are obtained by calculating difference of free energies between the undercooled liquid and the bcc

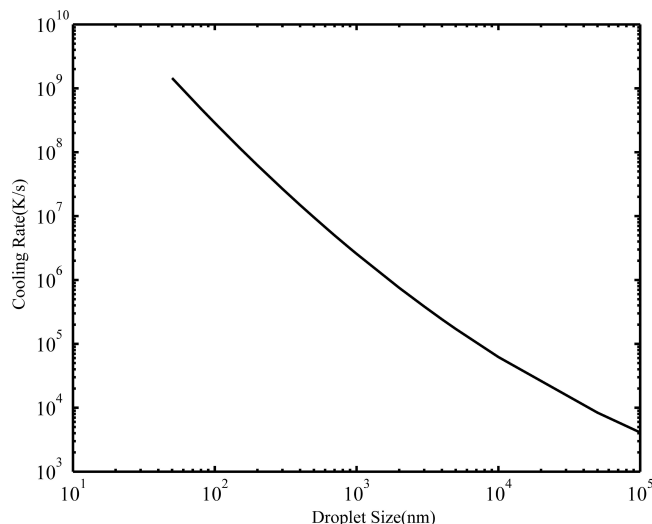


FIG. 9. Calculated cooling rate of droplets as a function of droplet size for Fe-25 at.% Ge composition.

solid solution. The experimental specific heat data for pure component of iron and germanium as given by Barin et. al.¹⁶ are used. The free energies of the undercooled liquids of pure components are calculated using Taylor series expansion of specific heat data as suggested by Lele et.al.¹⁷ For bcc solid solution, the free energy has been calculated using specific heat data obtained from Ref. ¹⁸. The free energy expressions and specific heat data of liquid are not available in literature. We have used the specific heat data of Fe–Si binary alloy of similar compositions.¹⁹ The nucleation rate of the bcc phase has been calculated using homogeneous nucleation rate expression according to Thomson and Spaepen.²⁰ The solid/liquid interfacial energy for different alloy compositions is estimated using available expression.²¹ The detectable nuclei concentration has been determined on the basis of resolution and magnification in the transmission electron microscope. For TEM observations in the present work, the value has been determined as 10^{15} cm⁻³. The critical cooling rate to avoid the nose of the TTT curve is taken as the difference between the liquidus temperature and the nose temperature divided by the time corresponding to the nose.

The calculated TTT curves of bcc phase of Fe-20 at.% Ge and Fe-25 at.% Ge compositions are shown in Fig. 10. The critical cooling rate to avoid the nucleation of bcc phase in Fe₈₀Ge₂₀ is found to be 3.7×10^9 Ks⁻¹. The value for Fe₇₅Ge₂₅ is about 2.6×10^9 Ks⁻¹. These values are of same order of magnitude. The cooling rate of the droplets of sizes smaller than 70 nm as estimated from heat transfer calculations show similar values ($\sim 10^9$ Ks⁻¹).

B. Ordering in alloy droplets

The results presented here allow us to make some conclusions about the nature of ordering process during

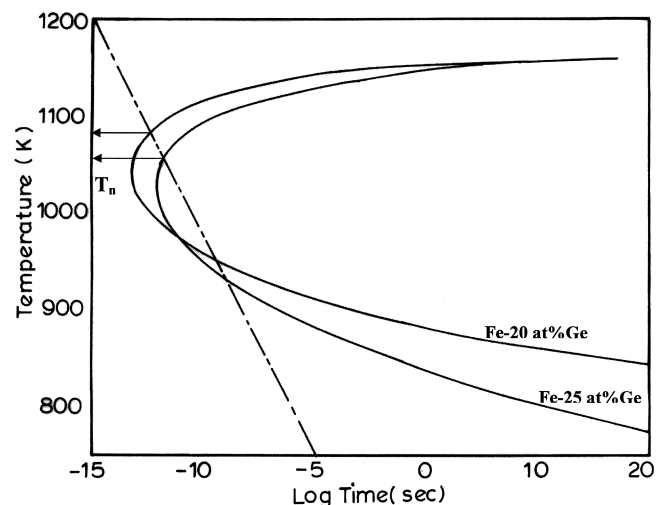


FIG. 10. TTT curves for homogeneous nucleation of the bcc phase for Fe-20 at.% Ge and Fe-25 at.% Ge alloy.

rapid solidification of the droplets. The diffraction evidence from smaller size droplets (<500 nm) clearly indicates absence of superlattice reflections. Thus solid solutions are disordered in nature. Since these droplets are iron rich, the direct nucleation of bcc α -FeGe phase is expected. However, the results suggest suppression of subsequent solid-state ordering. The droplets larger than 800 nm show ordering tendency. The compositions of these droplets are closer to Fe₃Ge composition. Thus, one expects the direct nucleation of α_2 (B2) phase from the melt in these droplets. The presence of B2 and DO₃ ordering can be clearly observed from the microdiffraction patterns. The dark-field imaging with the superlattice reflections, however, reveal extremely fine domain size. This suggests that ordering transformation has taken place in the solid state at lower temperature. Direct solidification of any ordered compound from the melt would reveal either very coarse domains or no domains. Therefore, the observed situation here corresponds to a disorder trapping during rapid solidification in which case the long-range order parameter goes to zero due to interface kinetics.

To explore the kinetic effect of solidification on ordering, it is necessary to estimate the growth rate of the solid–liquid interface. Boettinger et al.²² have given an analytical model for calculation of interface velocity during solidification of undercooled droplets. The model extends the work of Levi and Mehrabian,²³ who have calculated the interface position and velocity of an undercooled droplet subjected to external cooling when nucleation occurs on the surface of the droplets. To obtain the growth velocity V_r during recalescence in an initially undercooled droplet with no external cooling, Boettinger et al.^{22,24} used a heat balance approach and obtained a relationship assuming linear attachment kinetics as follows:

$$V_r = V_0 \left(1 - \frac{1}{\Delta\theta} \cdot \frac{x}{d} \right) \quad (7)$$

where V_0 is the initial growth rate, d is the diameter of the droplet, and $\Delta\theta$ is the dimensionless undercooling defined as $\Delta\theta = \Delta T C_p / L$. C_p is the heat capacity and L is the latent heat. For estimation of V_r , we need to know V_0 , the initial growth rate and ΔT . To estimate V_0 , we need to know velocity–undercooling relationship of Fe–25 at.% Ge alloy. In an earlier paper,⁷ we experimentally determined a relationship between undercooling (K) and growth velocity (ms^{-1}) for α -FeGe phase in undercooled Fe–25 at.% Ge alloy. This relationship is given by

$$V = 1.16 \times 10^{-6} (\Delta T)^{2.65} \quad (8)$$

Thus, the estimation of V_0 in the present case requires the knowledge of levels of undercooling the melt experienced prior to nucleation. In the present investigation,

Fig. 10 shows the way we have calculated the nucleation temperature (or level of undercooling). Let us consider an 800-nm-sized droplet, which is the largest droplet observed in TEM investigation. Figure 9 shows that the droplets of this size will cool at rate of 10^7 K/s. The cooling rate curve is plotted on the TTT curves in Fig. 10. The nucleation temperature is thus given by the intersection of the cooling curve with the TTT curves. The nucleation temperatures of the bcc α -FeGe for two different compositions are shown by black arrows. Therefore, the levels of undercooling obtained for Fe–25 at.% Ge and Fe–20 at.% Ge alloys are 453 and 493 K, respectively. One can notice that in the case of the Fe–25 at.% Ge alloy, the level of undercooling is quite close to the hypercooling temperature, whereas in the case of the Fe–20 at.% Ge alloy, it is higher than the hypercooling temperature. Using $\Delta T = 453$ K for the case of the Fe–25 at.% Ge alloy an estimated value of 12.5 ms^{-1} for V_0 is obtained. Similarly, $\Delta\theta$ is estimated to be 0.9293. If these data are transferred to Eq. (7), the estimated V_r is plotted against fractional solidified distance x/d for an 800-nm-sized droplet. Figure 11 shows the estimated growth velocity inside an 800-nm-sized droplet.

One can use disorder-trapping model by Boettinger and Aziz²⁵ to arrive at idea of critical velocity required for disorder trapping. The critical velocity, V_c is given by

$$V_c = V_D \left(\frac{T_c}{T_m} - 1 \right) \quad (9)$$

where V_D is the diffusive speed of atomic species involved, which is the ratio of the interface diffusivity (D) to the jump distance (a_0), T_c is the critical temperature for equilibrium order–disorder transition,²⁶ and T_m is the

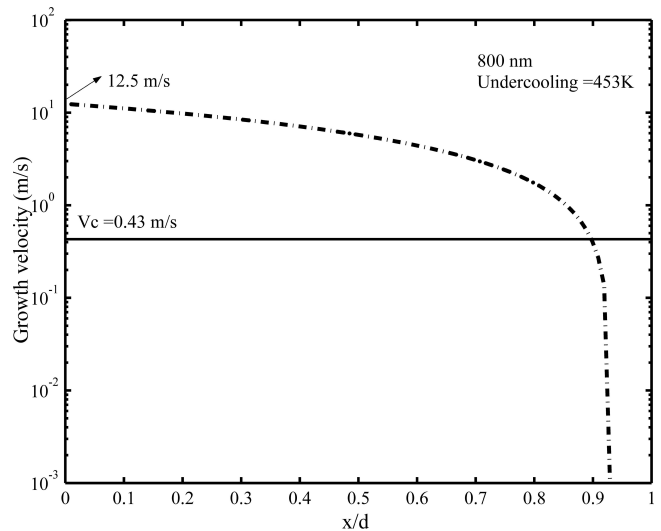


FIG. 11. Estimated growth velocity versus fractional distance across an initially undercooled 800-nm-sized droplet. The initial undercooling as estimated is 453 K below the liquidus line of α -FeGe and produces an initial growth rate of 12.45 m/s.

solidus temperature of the compound. Using phase diagram information of Fe–Ge, $T_C = 1513$ K, $T_M = 1393$ K, and $V_D = 5$ ms⁻¹, we obtain the critical velocity for disorder trapping, $V_c = 43$ cms⁻¹.

In Fig. 11, critical velocity (V_c) for disorder trapping as calculated using Eq. (9) is also plotted. One can find that velocity of solid–liquid interface (x) across the droplet diameter (d) is much higher than the critical velocity for disorder trapping. Therefore, the solid–liquid interface velocity in an 800-nm-sized droplet is such that growth of a disorder phase will be always favored. In the case of droplets having sizes less than 800 nm, the calculated interface velocity will be much higher than the critical velocity for disorder trapping. Subsequent ordering in the solid state depends on cooling rate. Our results show that only DO₃ ordering takes place for larger droplets, indicating a metastable extension of the DO₃ phase. We note that in a few particles, direct nucleation of the ϵ phase occurred. This is most likely due to segregation of heterogeneous nucleation sites in these droplets during fragmentation, which favors ϵ nucleation.

V. CONCLUSION

The present investigation establishes that the process of laser ablation of Fe–25 at.% Ge alloy leads to the formation atomized droplets of various sizes. The microstructure of the droplets exhibits a size dependent hierarchy of phases. At small sizes, the stoichiometry of the droplets fluctuates. However, the microstructure of the droplets below 70 nm suggests the predominance of only amorphous phase. A disordered bcc phase forms during solidification of droplets between 100 and 500 nm. For droplets larger than this range, a phase with ordered DO₃ structure predominates. However, one can also observe ϵ phase in some of the droplets. Our results suggest that the phase formation in the droplets is kinetically controlled through nucleation and growth. The observation of domain boundaries in larger droplets of near Fe₃Ge composition indicates the phenomenon of disorder trapping during solidification. The rapid solidification and consequent phase selection can be rationalized by invoking the prevailing heat transfer scenario to obtain an estimate of cooling rate followed by a calculation of growth velocity using continuous growth model. These estimated velocities exceed the critical velocity required for disorder trapping.

ACKNOWLEDGMENTS

The authors would like to acknowledge Aeronautical Research and Development Board (ARDB) and Defense Research and Development Organization (DRDO), India for their financial support.

REFERENCES

1. T.J. Jackson and S.B. Palmer: Oxide superconductor and magnetic metal thin film deposition by pulsed laser ablation: A review. *J. Phys. D: Appl. Phys.* **27**, 1581 (1994).
2. H. Yu, F.W. Froben, and M.G. Huber: Laser ablation of refractory materials, cluster formation and deposition. *Appl. Surf. Sci.* **86**, 74 (1995).
3. S. Bysakh, P.K. Das, and K. Chattopadhyay: Metastable microstructures in laser-ablation-deposited Al–Fe thin films. *Philos. Mag. A* **81**, 2689 (2001).
4. S. Bysakh, K. Mitsuishi, M. Song, K. Furuya, and K. Chattopadhyay: Transmission electron microscopy and high-resolution transmission-electron-microscopy study of nanostructure and metastable phase evolution in pulse-laser-ablation-deposited Ti–Si thin film. *J. Mater. Res.* **19**, 1118 (2004).
5. H. Dupond, J.P. Gavigan, D. Givord, A. Lienard, J.P. Rebouillat, and Y. Souche: Velocity distribution of micron-size particles in thin film laser ablation deposition (LAD) of metals and oxide superconductors. *Appl. Surf. Sci.* **43**, 369 (1989).
6. T.B. Massalaski: *Binary Alloy Phase Diagrams*, 2nd ed. (ASM International, Materials Park, OH, 1990), p. 1704.
7. G. Phanikumar, K. Biswas, O. Funke, D. Holland-Moritz, D.M. Herlach, and K. Chattopadhyay: Solidification of undercooled peritectic Fe–Ge alloy. *Acta Mater.* **53**, 3591 (2005).
8. Y-S. Kwan, K.B. Gerasimo, O.I. Lomovsky, and S.V. Pavlov: Steady state products in the Fe–Ge system produced by mechanical alloying. *J. Alloys Compd.* **359**, 194 (2003).
9. S. Bysakh: Development of laser ablation technique for production of intermetallic thin film and application to Al–Fe system. MSc.(Engg.) Thesis, Indian Institute of Science, Bangalore, India (1995).
10. J.I. Goldstein: *Introduction to Analytical Electron Microscopy*, edited by J.J. Hren, J.I. Goldstein, and D.C. Joy (Plenum, New York, 1979), p. 83.
11. R. Mehrabian: Rapid solidification. *Int. Metal Rev.* **27**, 185 (1982).
12. M. Pasandideh-Fard, R. Bhola, S. Chandra, and J. Mostaghini: Deposition of tin droplets on a steel plate: Simulations and experiments. *Int. J. Heat Mass Transfer* **41**, 2929 (1998).
13. M. Chung and R.H. Rangel: Parametric study of metal droplet deposition and solidification process including contact resistance and undercooling effect. *Int. J. Heat Mass Transfer* **44**, 605 (2001).
14. Z. Zhao and D. Poulidakos: Heat transfer and fluid dynamics during the collision of a liquid droplet on a substrate—I. Modeling. *Int. J. Heat Mass Transfer* **39**, 2771 (1996).
15. Y.S. Zouloukian and E.H. Buyco: *Thermophysical Properties of Matter*, The TPC Data Series, Vol. 5 (IFI/Plenum, New York, Washington, 1970).
16. I. Barin, O. Knacke, and O. Kubaschewski: *Thermochemical Properties of Inorganic Substances*, Supplement, (Springer, Berlin, Germany, 1977).
17. S. Lele, K.S. Dubey, and P. Ramchandrarao: On the temperature dependence of free energy of crystallization. *Curr. Sci.* **54**, 994 (1985).
18. V.E. Zinov'ev, L.D. Zangrebia, L.N. Petrova, and V.A. Sipailor: Electrical resistance and thermophysical properties of solid solution of germanium in iron. *Izvestiya Vysshikh Uchebnykh Zavendeii Fizika* **6**, 36 (1983).
19. R. Hultgreen, P.D. Desai, D.T. Hawkins, M. Gleiser, K.K. Kelley, and D.D. Wagman: Selected values of the thermodynamic properties of the elements (American Society for Metals, Cleveland, OH, 1973).
20. C.V. Thomson and F. Spaepen: Homogeneous crystal nucleation in binary metallic melts. *Acta Metall.* **31**, 2021 (1983).

21. F. Spaepen and R.B. Meyer: The surface tension in a structural model for the solid-liquid interface. *Scripta Metall.* **10**, 257 (1976).
22. W.J. Boettinger, L.A. Bendersky, and J.G. Early: An analysis of the microstructure of rapidly solidified Al-8Wt Pct Fe powder. *Metall. Trans.* **17A**, 781 (1986).
23. C.G. Levi and R. Mehrabian: Heat Flow during rapid solidification of undercooled metal droplets. *Metall. Trans.* **13A**, 13 (1982).
24. S.C. Sharma, T. Volkman, and D.M. Herlach: Microstructural development in drop-tube-solidified Al-3.6wt% Fe droplets: An analysis. *Mater. Sci. Eng.* **A171**, 169 (1993).
25. W. Boettinger and M.J. Aziz: Theory for the trapping of disorder and solute in intermetallic phases by rapid solidification. *Acta Metall.* **37**, 3379 (1989).
26. M.J. Aziz: Interface attachment kinetics in alloy solidification. *Metall. Trans.* **27A**, 671 (1996).